ISSN 1674-1056
http://cpb.iphy.ac.cn
http://iopscience.iop.org/cpb
中国物理 B
Chinese Physics
中国物理 Chinese Physics B

Ramsey-coherent population trapping Cs atomic clock based on lin||lin optical pumping with dispersion detection

Peng-Fei Cheng(程鹏飞), Jian-Wei Zhang(张建伟), Li-Jun Wang(王力军)

Citation: Chin. Phys. B . 2019, 28(7): 070601. **doi:** 10.1088/1674-1056/28/7/070601
Journal homepage: http://cpb.iphy.ac.cn; http://iopscience.iop.org/cpb

What follows is a list of articles you may be interested in

Development of the integrated integrating sphere cold atom clock

Ming-Yuan Yu(于明圆), Yan-Ling Meng(孟艳玲), Mei-Feng Ye(叶美凤), Xin Wang(王鑫), Xin-Chuan Ouyang(欧阳鑫川), Jin-Yin Wan(万金银), Ling Xiao(肖玲), Hua-Dong Cheng(成华东), Liang Liu(刘亮)

Chin. Phys. B . 2019, 28(7): 070602. **doi:** 10.1088/1674-1056/28/7/070602

Photonic generation of RF and microwave signal with relative frequency instability of 10^{-15}

Lu-Lu Yan(闫露露), Wen-Yu Zhao(赵文宇), Yan-Yan Zhang(张颜艳), Zhao-Yang Tai(邰朝阳), Pan Zhang(张攀), Bing-Jie Rao(饶冰洁), Kai Ning(宁凯), Xiao-Fei Zhang(张晓斐), Wen-Ge Guo(郭文阁), Shou-Gang Zhang(张首刚), Hai-Feng Jiang(姜海峰)

Chin. Phys. B . 2018, 27(3): 030601. **doi:** 10.1088/1674-1056/27/3/030601

Evaluation of the frequency instability limited by Dick effect in the microwave $^{199}Hg^{+}$ trapped-ion clock

Yi-He Chen(陈义和), Lei She(佘磊), Man Wang(汪漫), Zhi-Hui Yang(杨智慧), Hao Liu(柳浩), Jiao-Mei Li(李交美)

Chin. Phys. B . 2016, 25(12): 120601. **doi:** 10.1088/1674-1056/25/12/120601

Microwave interrogation cavity for the rubidium space cold atom clock

Wei Ren(任伟), Yuan-Ci Gao(高源慈), Tang Li(李唐), De-Sheng Lü(吕德胜), Liang Liu(刘亮)

Chin. Phys. B . 2016, 25(6): 060601. **doi:** 10.1088/1674-1056/25/6/060601

Recent improvements on the atomic fountain clock at SIOM

Du Yuan-Bo, Wei Rong, Dong Ri-Chang, Zou Fan, Wang Yu-Zhu

Chin. Phys. B . 2015, 24(7): 070601. **doi:** 10.1088/1674-1056/24/7/070601

Ramsey-coherent population trapping Cs atomic clock based on lin||lin optical pumping with dispersion detection*

Peng-Fei Cheng(程鹏飞)[1,2], Jian-Wei Zhang(张建伟)[2,3,†], and Li-Jun Wang(王力军)[1,2,3,‡]

[1] *Department of Physics, Tsinghua University, Beijing* 100084, *China*
[2] *State Key Laboratory of Precision Measurement Technology and Instruments, Tsinghua University, Beijing* 100084, *China*
[3] *Department of Precision Instruments, Tsinghua University, Beijing* 100084, *China*

(Received 22 March 2019; revised manuscript received 10 April 2019; published online 21 May 2019)

A Cs vapor cell-based atomic clock that uses a lin||lin pumping scheme with dispersion detection is reported. This atomic clock shows potential for high performance because of its high contrast pumping scheme, and for miniaturization because of its simple architecture. The experimental setup and optimal operating parameters for the clock are introduced. The current fractional frequency stability is measured to be $1.3\times10^{-12}/\sqrt{\tau}$ up to 20 s and reaches 3.1×10^{-13} at 200 s. We have thoroughly investigated the related noise sources that affect clock frequency stability at the 1 s and 100 s levels. The investigation shows that the laser frequency noise limits the clock frequency stability significantly. The clock performance can be further improved by technically upgrading the laser frequency stabilization setup.

Keywords: Ramsey-coherent population trapping (CPT) atomic clock, frequency stability, noise analysis

PACS: 06.30.Ft, 06.20.-f, 95.55.Sh **DOI:** 10.1088/1674-1056/28/7/070601

1. Introduction

Vapor cell-based microwave atomic clocks are well adapted for use as secondary frequency standards in various applications. Lamp-pumped Rb atomic clocks are widely used in global navigation satellite system (GNSS) applications,[1] telecommunications, and defense equipment. In recent years, high-performance atomic clocks that are compact in size and offer reasonable power consumption have been in strong demand. As the performance levels of the laser sources continue to increase, multiple novel laser pumping and interrogation schemes and techniques are being actively studied in laboratories worldwide to reduce the volume and power consumption, or to improve the frequency stability, of these clocks. Schemes based on the coherent population trapping (CPT) phenomenon have turned out to be among the most promising approaches to the development of compact clocks.[2] Unlike the traditional microwave double resonance clock, the microwave cavity can be removed from a CPT atomic clock.

Since the first demonstration of the technique using a sodium atomic beam,[3] CPT-based atomic clock research has become increasingly productive. Several types of optimized pumping schemes have been developed for both continuous wave (CW) and pulsed operation.[4–7] To overcome the low contrast that constitutes the main drawback of the traditional CW CPT clock, techniques such as polarization modulation have been reported in the literature,[4,8,9] with other examples included in the references cited therein. One of the best frequency stabilities achieved in the CW region by applying a polarization modulation technique showed the good result of $3.2\times10^{-13}/\sqrt{\tau}$ up to 100 s.[4] However, traditional CW region CPT clocks tend to suffer from significant CPT line-power broadening and light-induced frequency shifts. A promising alternative option is to operate the clock in pulsed mode to introduce the Ramsey method of separated oscillating fields. The Ramsey-CPT can effectively reduce the fringe linewidth, which is dependent on the free evolution time rather than the laser power. In addition, another significant advantage of the Ramsey-CPT is that light-induced frequency shifts can be suppressed by simply using different interrogation periods; this is called autobalanced Ramsey (ABR) spectroscopy.[10] Therefore, the medium-term and long-term performances of these clocks are promising. Several innovative pumping schemes, including the lin⊥lin,[5] lin||lin,[6] and push-pull optical pumping (PPOP)[7,11] schemes, have been demonstrated to obtain high contrast. Recently, the state-of-the-art performance of a PPOP CPT atomic clock with a frequency stability of $3\times10^{-13}/\sqrt{\tau}$ up to 2000 s was achieved at Laboratoire National de Métrologie et d'Essais-Systèmes de Référence Temps-Espace (LNE-SYRTE)[12] by implementation of the ABR technique.

The lin||lin scheme has been studied with the main focus on the CW CPT clock, in which the frequency stability remains at approximately $2\times10^{-11}/\sqrt{\tau}$ up to only 20 s.[8] However, to the best of our knowledge, no pulsed CPT

*Project supported by the National Key Research and Development Progress of China (Grant No. 2016YFA030210) and the Initiative Program of the State Key Laboratory of Precision Measurement Technology and Instruments, China.

†Corresponding author. E-mail: zhangjw@tsinghua.edu.cn
‡Corresponding author. E-mail: lwan@tsinghua.edu.cn

© 2019 Chinese Physical Society and IOP Publishing Ltd

atomic clocks using the lin||lin scheme have been reported in the literature. Theoretically, the lin||lin scheme shows more advantages for miniaturization when compared with the well-developed lin⊥lin scheme because the two interacting, parallel-polarized, and coherent frequency laser beams can be generated easily via an electro-optical modulator (EOM). However, the lin||lin scheme provides a way to implement dispersion detection, which further improves the contrast,[13–15] whereas the lin⊥lin scheme usually requires the use of two phase-locked lasers or a Michelson interferometer to generate the perpendicular polarized laser beams. We have been developing a Cs atomic clock based on lin||lin Ramsey-CPT in our laboratory over the last two years.[13,16] In this paper, we report the performance achieved by this lin||lin Ramsey-CPT atomic clock and describe our in-depth investigation of the current limitations of this clock.

In Section 2, the experimental setup will be described and the related parameter optimization steps will be discussed. In Section 3, the experimental results are presented and the frequency stability limitations at averaging times of 1 s and 100 s will be analyzed. Conclusions are drawn in the final section.

2. Experimental setup

A schematic diagram of the experimental setup, which mainly includes the optical components, the Cs vapor cell's physical parts, and the electronic parts, is shown in Fig. 1. We have thoroughly optimized the parameters related to this setup, including the laser frequency and power, the vapor cell temperature, the static magnetic field (the C-field), the operating time sequences, and the 9.2 GHz radio-frequency (RF) power.

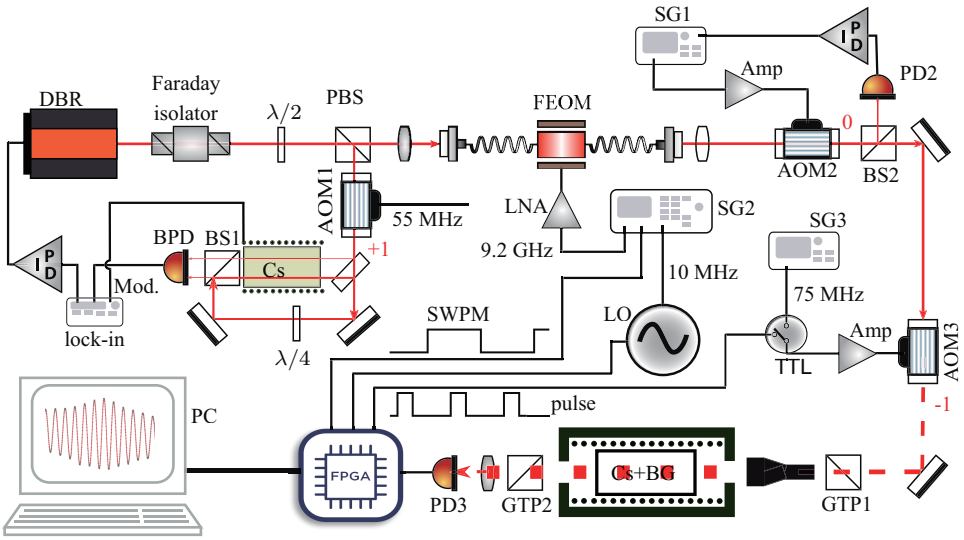


Fig. 1. Schematic of experimental setup. DBR: distributed Bragg reflector laser. PBS: polarizing beam splitter. BS: beam splitter. FEOM: fiber electro-optic modulator. AOM: acousto-optical modulator. SG: signal generator. Amp: microwave power amplifier. PD: photodetector. BPD: balanced photodetector. LNA: low-noise amplifier. $\lambda/2$ and $\lambda/4$: half-wave and quarter-wave plates, respectively. TTL: transistor-transistor logic switch. PID: proportional-integral-derivative controller. FPGA: field-programmable gate array. BG: buffer gas. LO: local oscillator. SWPM: square-wave phase modulation. Mod.: lock-in amplifier modulation signal applied to the solenoid. GTP: Glan–Taylor polarizer. BG: buffer gas.

2.1. Optical setup

A distributed Bragg reflector (DBR) laser is used to generate the 894.5 nm laser beam required to pump the Cs atoms. A small part of this laser output is split from the main beam to stabilize the frequency. Before the laser beam is directed into the saturable absorber, the laser frequency is shifted by +55 MHz using an acousto-optical modulator (AOM); it is then stabilized to the $|6^2S_{1/2}, F = 4\rangle \rightarrow |6^2P_{1/2}, F' = 3\rangle$ transition of the Cs D_1 line using the nonbackground saturated absorption (SA) method via balanced detection. The laser frequency error is obtained from a lock-in amplifier using Zeeman modulation through a solenoid located around the vapor cell.

The coherent CPT resonant bichromatic laser is then generated using a fiber electro-optical modulator (FEOM). We use the carrier and the +1st order sideband to pump the atoms into the CPT dark state; the 9.2 GHz driven microwave thus refers to the clock transition. Given that the laser power noise is known to be one of the main noise sources that limit the clock performance,[17–19] a laser power stabilization loop has been designed by controlling the AOM-driven RF power. To implement the Ramsey method,[20] the laser is switched using the −1st order diffraction beam of AOM3, which is driven using a pulsed microwave signal at 75 MHz. The total laser frequency shift required to compensate for the buffer gas-induced frequency shift is −130 MHz, as shown in Fig. 2. Two near-orthogonal Glan–Taylor polarizers are set before and after the clock cell to implement dispersion detection.[14] The pulsed laser beam is expanded up to a diameter of 12 mm to excite as many atoms into the CPT dark state as possible. Finally,

the transmitted laser beam, which contains the clock transition signal, is detected using photodetector 3 (PD3).

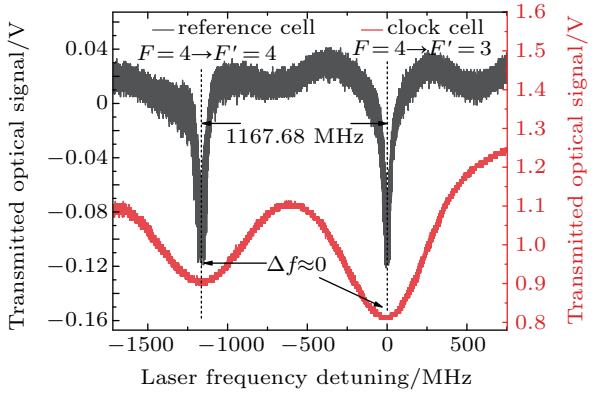


Fig. 2. Doppler-free absorption spectra of Cs D_1 line in the nonbuffered reference cell (upper black line) and the buffered clock cell (lower red line). The clock cell spectra record the bichromatic laser absorption characteristics. The two absorptions correspond to excited levels $|6^2P_{1/2}, F'=4\rangle$ and $|6^2P_{1/2}, F'=3\rangle$, as marked.

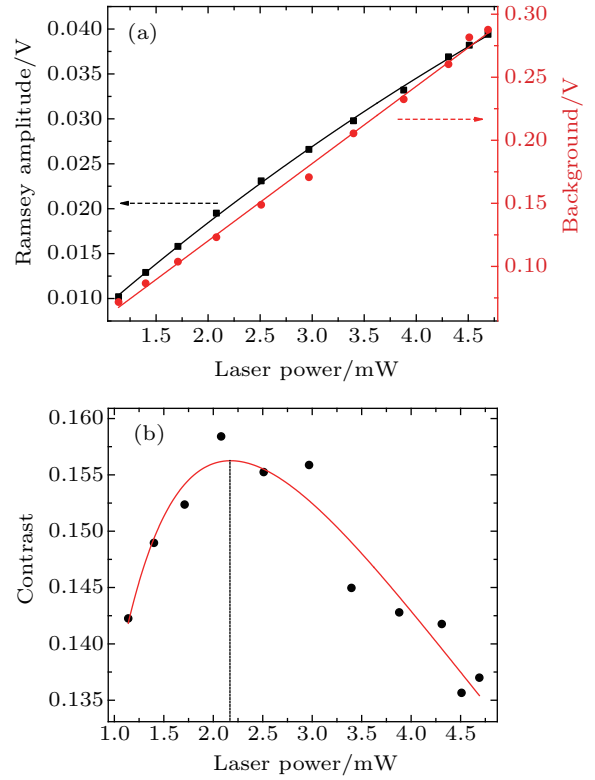


Fig. 3. Laser power optimization. (a) The Ramsey amplitude (black squares and black exponential fitted line) and the background (red dots and red linear fitted line) are dependent on the laser power exponentially and linearly, respectively. (b) Similarly, the calculated contrast (black dots) is well fitted using an exponent function that is divided by a linear function (red line). The optimal laser power is measured to be 2.2 mW.

The laser power stabilization loop is shown in Fig. 1. A 3:7 beam splitter (BS) is used to split 3/10 of the laser power into PD2 (PDA36EC, Thorlabs), and the signal is then fed to an analog proportional-integral-derivative (PID) module (LB1005, Newfocus). By adjusting the RF drive power of AOM2 through the amplitude modulation (AM) input of signal generator 1 (SG1), the laser power is stabilized to the set-point. An out-loop PD, which is not shown in Fig. 1, is placed temporarily behind BS2 to monitor the power fluctuations of the locked output laser. The working laser power affects the amplitude and background of the Ramsey signal and thus affects the contrast, as shown in Fig. 3. As expected, the amplitude increases exponentially with laser power increasing while the background increases linearly. The optimal laser power to maximize the contrast is measured to be 2.2 mW, as shown in Fig. 3(b).

As reported in Ref. [14], the angle of the two Glan–Taylor polarizers θ affects the contrast of Ramsey signal significantly because of the use of the lin$\|$lin scheme and the dispersion detection. The relationship between the contrast and θ is given by

$$C(\theta)=\frac{\phi(B)I_{\mathrm{CPT}}\theta}{\kappa I_{\mathrm{total}}\theta^2}, \tag{1}$$

where the numerator and the denominator represent the Ramsey amplitude and the background, respectively, ϕ is the polarization rotation angle of the resonant laser caused by the Faraday effect and is dependent on the applied magnetic field B, I_{CPT} and I_{total} are the intensities of the CPT resonant laser component and all components, respectively, and κ is a constant. The measured data and the fitted lines are shown in Fig. 4(a). The optimal θ is found to be $-4°$.

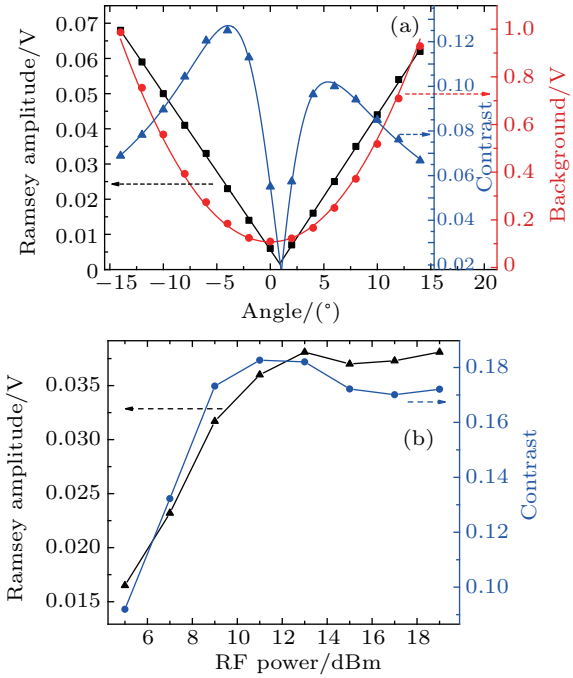


Fig. 4. (a) Optimization of the angle of the two Glan–Taylor polarizers. The Ramsey amplitude (black squares and black linear fitted line) and the background (red dots and red quadratic fitted line) are dependent on the angle linearly and quadratically, respectively. The optimal angle $\theta=-4°$, according to the maximal contrast (blue triangles and fitted line). (b) Optimization of the 9.2 GHz RF power. The optimal RF power is measured to be 10 dBm.

The relative intensity of the two-frequency CPT laser is determined from the RF power that is applied to the FEOM

and is also an important parameter. We have measured the Ramsey amplitude and the contrast trends in the RF power. As shown in Fig. 4(b), the contrast and the amplitude turn out to be saturated over 10 dBm, which is thus the optimal value.

2.2. Cs vapor cell physical package setup

The vapor cell physical package includes a glass cell, a three-layer magnetic shield to eliminate the effects of geomagnetic field fluctuations, a solenoid to generate a C-field, and a nonmagnetic heater to control the cell temperature. The clear aperture of the package is 15 mm in diameter. As shown in Fig. 5(b), the physical package has a layered structure and the following components are set from the innermost to the outermost layers: glass vapor cell, internal nonmagnetic heater, C-field solenoid, teflon-made temperature isolator, and three-layer magnetic shields.

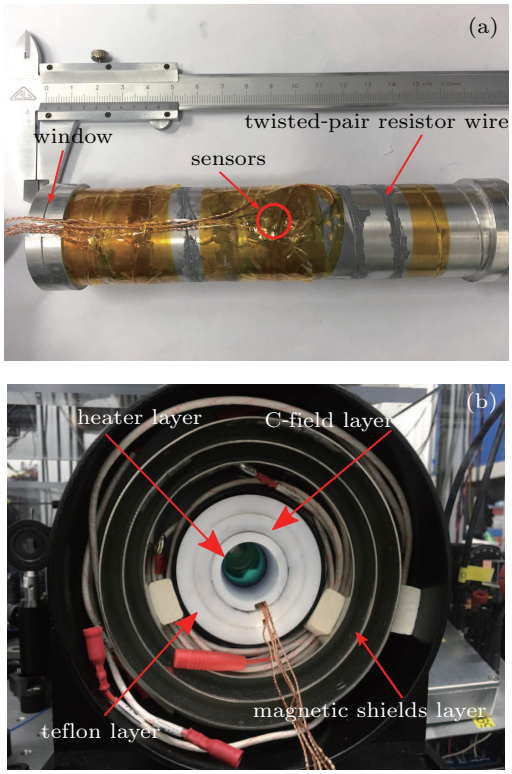


Fig. 5. Vapor cell package, including (a) the nonmagnetic heating setup and (b) the assembled setup, where the clear package aperture is 15 mm in diameter.

The clock core is a cylindrical glass cell of diameter $D = 28$ mm and length $L = 30$ mm. The Cs metal is filled with a mixed N_2 and Ar buffer gas to minimize the temperature coefficient of the collision-induced frequency shift. The total buffer gas pressure P_{buffer} is 2.33 kPa at a ratio of $P_{N_2}/P_{\text{Ar}} = 0.55$, which has been designed to eliminate the temperature-to-frequency-shift sensitivity that occurs at 38 °C, according to Ref. [21].

The temperature control setup is shown in Fig. 5(a). To provide a uniform thermal environment, we place the Cs vapor at the center of a hollow aluminum cylinder. A 0.2-mm-diameter constantan twisted-pair wire is twined within the groove and is sealed with heatsink silicone grease to heat the entire aluminum cylinder. A 13 kHz alternating current (AC) is applied to heat the twisted-pair wire. The magnetic fluctuations induced by this heating current are too small (under 0.1 nT resolution) to be measured using a fluxgate in a 1 Hz bandwidth. Coated windows are used to cover each end of the cylinder to isolate the heat flow. Two negative temperature coefficient resistors (NTC203LE, Vishay) are placed through a hole to be close to the vapor cell, as indicated in Fig. 5(a). The temperature sensitivity is approximately 320 °C/Ω around 37 °C. Two Teflon cylindrical layers are arranged outside the heating package to act as thermal isolators, and the inner layer carries a solenoid to generate the C-field. Two bridge circuits are used to monitor the resistance changes. The output voltages from the bridge circuits are amplified and are then sampled using analog-to-digital converters (ADCs). One of the circuits is used to lock the temperature via a digital PID controller, while the other is used as the out-loop monitor to measure the temperature. The maximum heating power of approximately 15 W is limited by the output power of the home-made controller. The measured temperature fluctuation is below 1 mK in 1 h, which contributes approximately 3×10^{-13} at 1000 s to the clock frequency stability. As shown in Fig. 6(a), the amplitudes of the Ramsey fringes increase along with increasing temperature because of the increasing numbers of atoms. However, the higher temperature also increases the optical thickness, which then reduces the transmitted optical power. As a compromise, the optimal cell temperature is set at 37.5 °C.

The three-layer permalloy magnetic shield rejects the external longitudinal magnetic field fluctuations by a factor of 10000 along the z-axis. The geomagnetic fluctuations in a 1000 s period are guaranteed to be sufficiently reduced from the 10 nT level to 1 pT approximately, which means that these fluctuations are negligible in our clock. A solenoid is placed on a Teflon cylinder to generate a C-field that is aligned with the cell axis (z-axis). In dispersion detection, the C-field value is an important parameter, as we reported previously in Ref. [14]. The ratio of the current to the magnetic field is measured to be 2.346 μT/mA. The current stability contributes to the clock frequency stability being below 1×10^{-13} at 1 s. As a consequence of the use of the lin||lin scheme and dispersion detection, the Ramsey amplitude changes periodically depending on the C-field, as shown in Fig. 6(b). The optimal magnetic value is set at 10 μT.

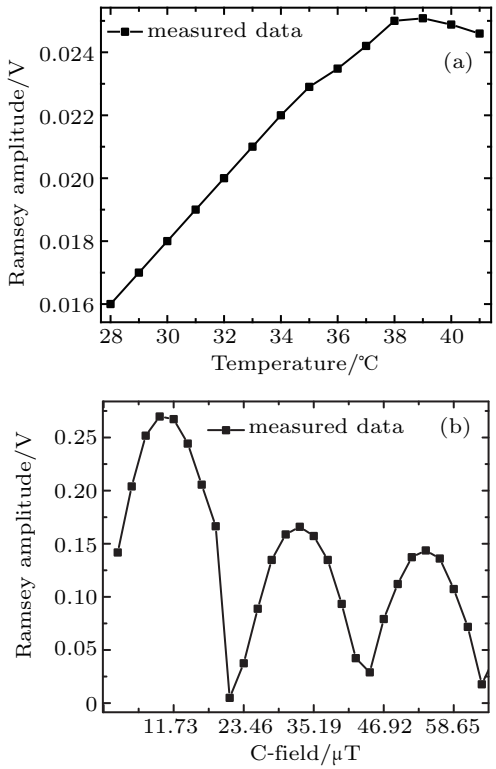


Fig. 6. (a) Optimization of the cell temperature. The optimal cell temperature is measured to be 37.5 °C. (b) Optimization of the C-field. The optimal C-field value is measured to be 10 μT.

2.3. Electronics setup

As shown in Fig. 1, the electronic architecture includes microwave generation modules and a field-programmable gate array (FPGA)-based electronic controller. The analog signal generator SG2 (E8257D, Keysight), which is referenced to the 10 MHz local oscillator (LO), is used to generate the 9.192 GHz microwave signal required by the CPT interaction scheme. We have measured the phase-noise power spectral density $S_\phi(y)$ of the 9.2 GHz signal, which shows that the microwave phase noise contribution to the clock frequency stability through the Dick effect[22] is $5\times10^{-13}/\sqrt{\tau}$.

The clock operation and data acquisition functions are performed by an FPGA-based electronic controller (USB-7855R, National Instruments) that was previously introduced.[24] A schematic of the clock's operating sequence is shown in Fig. 7(a). The Ramsey-CPT clock operates using the following three phases: (i) laser optical pumping of the atoms into the CPT dark state; (ii) free evolution with the input laser switched off; and (iii) detection of the clock transition at the beginning of the subsequent laser pulse. The clock frequency error is obtained by comparing the two points at the half-maximum on the left (L) and right (R) sides, as shown in Fig. 7(b). The phase of the 9.2 GHz microwave signal is modulated using a square wave to ensure that adjacent laser pulses are in different microwave phases. R_k and L_k are the kth detected signals when the phase differences between the pump pulse and the detection pulse are $+90°$ (pump: 0°; detection: 90°) and $-90°$ (pump: 90°; detection: 0°), respectively. The Ramsey fringes for the phase changes of $+90°$ and $-90°$ are shown in Fig. 7(b). When the frequency of the 9.2 GHz microwave signal is exactly resonant with the atoms, the detected L_k and R_k are located at the half-maximum on each side of the signal. Therefore, the clock frequency error is calculated to be

$$ERR_k(\nu) = R_k - L_k \tag{2}$$

in the kth detection, and

$$ERR_{k+1}(\nu) = -(L_{k+1} - R_k) \tag{3}$$

in the $(k+1)$th detection.

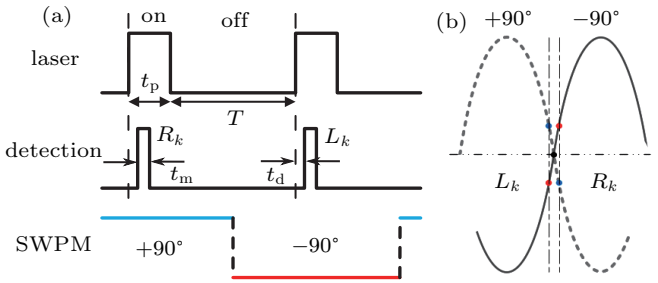


Fig. 7. (a) Operating time sequence of the Ramsey-CPT atomic clock. Laser: TTL trigger of the RF switch to turn the laser pulses on (high-voltage level) and off (low-voltage level) via AOM3. t_p and T are the periods when the laser pulses are turned on and off, respectively. Detection: sampling trigger of the Ramsey signal detected using PD3, which lasts for a period $t_m = 16$ μs. τ_d is a 500 ns delay used to ensure that the laser pulse is switched on. SWPM: the 9.2 GHz microwave signal is phase-modulated by a square wave via the built-in phase modulation function where the neighboring laser pulses alternate between $-90°$ (red) and $+90°$ (blue). (b) Central Ramsey fringes with square wave phase modulation at phases of $-90°$ (solid line) and $+90°$ (dashed line) used to obtain the left and right sides at half-linewidth points L and R, respectively.

The atoms are trapped in the dark state when the laser is switched on, exhibiting the exponential process shown in Fig. 8(a), and t_p is selected to be 500 μs. The well-known equation for the clock's short-term frequency stability can be written as

$$\sigma_y(\tau) = K\frac{\Delta\nu}{SNR\cdot\nu_0}\tau^{-1/2} \propto \frac{\Delta\nu}{Amp}, \tag{4}$$

where K is a constant, $\Delta\nu$ is the full width at half maximum (FWHM) of the signal, ν_0 is the clock transition frequency, SNR is the signal-to-noise ratio, and Amp is the signal amplitude. Therefore, reducing $\Delta\nu/Amp$ will improve the frequency stability performance. As Fig. 8(b) shows, the optimal free evolution period T is measured to be 2 ms in our setup, so the cycle time $T_C = T + t_p = 2.5$ ms. t_m and t_d are set to be 16 μs and 500 ns, respectively.

As a brief conclusion to this section, the optimal parameters obtained using our experimental setup are listed in Table 1. Under the optimal conditions, the contrast is measured to be 18%.

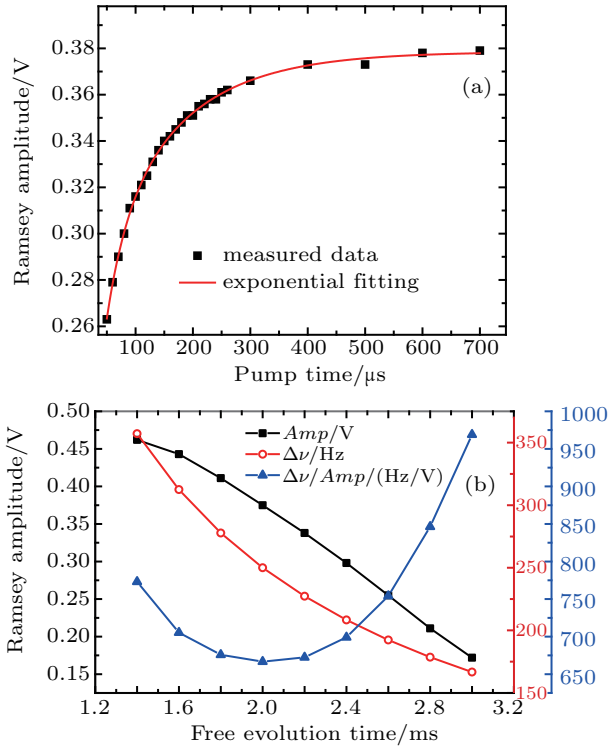


Fig. 8. Optimization of the optical pumping and free evolution periods of times t_p and T. (a) Black squares represent the measured amplitude of the Ramsey signal (*Amp*) for different pumping times, while the red solid line represents the exponential fitting. (b) Black squares represent the measured amplitudes of the Ramsey signal at different free evolution times, where the amplitude decreases with increasing T because of the decoherence of the dark state. The red circles represent $\Delta\nu$, which is approximately $1/2T$. The blue triangles represent the calculated values of $\Delta\nu/Amp$. The lines drawn in panel (b) are simply connections between the dots. The optimal t_p and T values are measured to be 500 μs and 2 ms, respectively.

Table 1. Measured optimal parameters.

Parameter	Value
Laser power	2.2 mW
Angle θ	−4°
Cell temperature T	37.5 °C
C-field B	10 μT
RF power	13 dBm
Pumping time τ_p	500 μs
Free evolution time T	2 ms

3. Results and discussion

3.1. Measured clock frequency stability

The measured frequency stabilities of the locked clock and the free-running LO are illustrated in Fig. 9. The measurements are acquired using a phase noise test set (5120A, Microsemi) that is referenced to an H-maser (MHM-2010, Microsemi). The LO is an oven-controlled crystal oscillator (OCXO) with frequency stability measured to be approximately 1.6×10^{-12} at 1 s before deteriorating to 4.6×10^{-12} at 200 s. When the LO is locked, the frequency stability is measured to be $1.3\times10^{-12}/\sqrt{\tau}$ up to 20 s. Because the clock is limited by other noises, the frequency stability reaches a value of 3.1×10^{-13} at $\tau=200$ s. To address the Allan deviation in Fig. 9, a linear drift of $6.8\times10^{-18}\tau$ has been removed from the locked data.

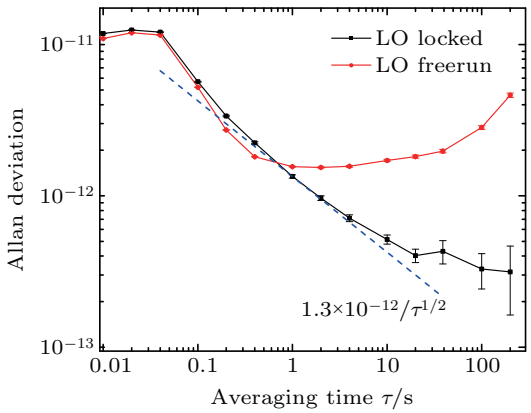


Fig. 9. Measured clock frequency stability. The red dots and line are the measured frequency stability of the free-running LO, which is approximately 1.6×10^{-12} at 1 s, and then deteriorates to 4.6×10^{-12} at 200 s. The LO-locked frequency stability (black squares and line) is measured to be $1.3\times10^{-12}/\sqrt{\tau}$ up to 20 s and then reaches the flick floor, which is approximately 3.1×10^{-13}. Note here that a linear drift of $6.8\times10^{-18}\tau$ has been removed.

3.2. Analysis of frequency stability limitations

To provide physical insight into the effects that lead to the measured results, we have investigated the main noise sources, which include shot noise, the LO phase noise, laser frequency noise, laser intensity noise, and thermal and magnetic noises.

First, we consider the shot noise of detected photons, for which the contribution to the clock frequency stability in terms of the Allan deviation can be expressed as[23]

$$\sigma_y^{\rm sn}(\tau)=\frac{\Delta\nu}{\pi\nu_0 C\sqrt{\eta_{\rm q}N_{\rm F}}}\sqrt{\frac{T_{\rm c}}{\tau}}, \tag{5}$$

where $\eta_{\rm q}=0.7$ is the quantum efficiency of the photodetector, and $N_{\rm F}=2.88\times10^9$ is the number of photons that reach the photodetector during our operation. This gives the result that $\sigma_y^{\rm sn}(\tau)=4.3\times10^{-14}/\sqrt{\tau}$.

Another important noise source in atomic clocks when operating in the pulsed mode is the phase noise of the interrogated microwave signal, which affects the clock signal through the Dick effect.[22] This can be described using the following well-known equation:[24]

$$\sigma_y^{\rm Dick}(\tau)=\left\{\sum_{k=1}^{\infty}{\rm sinc}^2\left(k\pi\frac{T}{T_{\rm c}}\right)S_y^{\rm LO}(kf_{\rm c})\right\}^{1/2}\tau^{-1/2}, \tag{6}$$

where $S_y^{\rm LO}(f)$ is the power spectral density of the microwave fractional frequency fluctuations, and $f_{\rm c}=1/T_{\rm c}$. $S_y^{\rm LO}(f)=S_\phi^{\rm LO}(f)f^2/\nu_0^2$, where $S_\phi^{\rm LO}(f)$ is the measured single-sideband phase noise. As shown in Fig. 10(a), the phase noise is fitted as follows:

$$S_{\phi}^{\mathrm{LO}}(f)=\begin{cases}1.35\times10^{-9}, & f=400\ \mathrm{Hz},\\ 2.03\times10^{-10}, & f=800\ \mathrm{Hz},\\ 1.33\times10^{-12}f^{2}-1.79\times10^{-8}f+3.26\times10^{-4}-0.29672f^{-1}+190.22f^{-2}, & 1\ \mathrm{kHz}\le f\le 106\ \mathrm{kHz},\\ 5.10\times10^{-14}f^{2}-4.33\times10^{-8}f-0.03+85975.88f^{-1}-1.05\times10^{10}f^{-2}, & 106\ \mathrm{kHz}<f\le 1\ \mathrm{MHz}.\end{cases} \tag{7}$$

Therefore, the Dick effect results in $\sigma_y^{\mathrm{LO}}(\tau)=5.1\times10^{-13}/\sqrt{\tau}$.

Laser power fluctuations are one of the main noise sources that affect the clock's frequency stability. In clocks in pulsed operation, the contribution of the laser power noise to the clock's Allan deviation can be expressed in a manner similar to the Dick effect as[23]

$$\sigma_y^{\mathrm{AM}}(\tau)=\frac{\Delta\nu}{C\nu_0}\left\{\sum_{k=1}^{\infty}\mathrm{sinc}^2\left(k\pi\frac{T}{T_{\mathrm{c}}}\right)S_{\mathrm{AM}}(kf_{\mathrm{c}})\right\}^{1/2}\tau^{-1/2}, \tag{8}$$

where $S_{\mathrm{AM}}(f)$ is the power spectral density of the fractional intensity fluctuations of the incident laser beam detected using the photodetector. In practice, the detected laser power noise contains both intrinsic relative intensity noise (RIN), which is called AM–AM noise, and the laser frequency-to-amplitude noise, which is called FM–AM noise.[25,26] We have measured $S_{\mathrm{AM}}(f)$ to be $1.3\times10^{-9}/\mathrm{Hz}^{-1}$ at 400 Hz, $4.5\times10^{-10}/\mathrm{Hz}^{-1}$ at 800 Hz, and approximately $1.0\times10^{-10}/\mathrm{Hz}^{-1}$ within the range from 1 kHz to 10 kHz after the laser beam is transmitted from the cell; this represents the sum of the AM–AM and FM–AM noises and the electronic noise, as shown in Fig. 10(b). The contribution of the laser power noise is derived to be $\sigma_y^{\mathrm{AM}}(\tau)=1.5\times10^{-12}/\sqrt{\tau}$. Specifically, the FM–AM noise dominates the laser intensity noise, as shown in Fig. 10(b), because the off-resonance laser intensity noise is far lower than the on-resonance laser intensity noise.

In addition to the noise contributions discussed above, the laser frequency and intensity fluctuations, the cell temperature fluctuations, and the magnetic fluctuations all affect the clock frequency stability via the light shift, the collisional frequency shift, and the quadratic Zeeman shift, respectively. These fluctuations are more significant in terms of medium-term and long-term performance, which is discussed in the following. First, the light shift is investigated from the practical viewpoint that the effective light shift can be regarded as a laser intensity-induced frequency shift and a laser frequency detuning-induced frequency shift. We have measured the impact slopes of the laser frequency and intensity experimentally.

To measure the laser frequency stability, an extra DBR laser system that is locked to the Cs $|6^2\mathrm{S}_{1/2},F=4\rangle\rightarrow|6^2\mathrm{P}_{1/2},F'=3\rangle$ atomic transition is built. We then measure the beat signal of the two frequency-stabilized laser beams using a 150-MHz-bandwidth photodetector (PDA10CF, Thorlabs). Because the workhorse laser is locked −55 MHz away from the atomic transition, the beat signal after passing through a low-pass filter is sinusoidal at 55 MHz, and this signal is then measured using a frequency counter (53220A, Keysight). Assuming that the frequency noises of the two laser beams are similar but independent, each of these noises is estimated to be $1/\sqrt{2}$ of the measured stability. As shown in Fig. 11(a), the frequency stability reaches 8.9×10^{-11} at 1 s and 6.8×10^{-11} at 100 s. The slope of the clock frequency shift versus the laser frequency detuning characteristic is measured by varying the drive frequency of AOM3. The slope is determined to be −201 mHz/MHz, as shown in Fig. 11(b). Therefore, the laser frequency-induced frequency limitation is 4.5×10^{-13} at 1 s and 3.5×10^{-13} at 100 s.

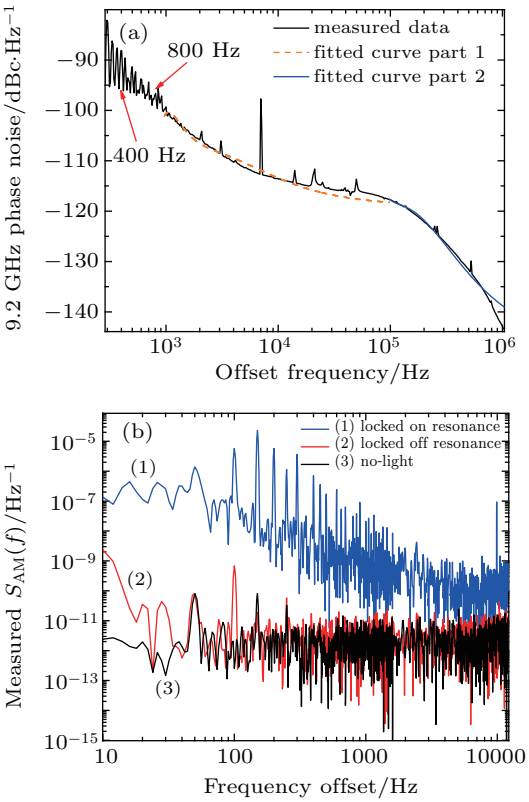


Fig. 10. (a) Single-sideband phase noise of the 9.2 GHz microwave synthesizer (black solid line) measured using a signal source analyzer (E5052B and E5053A, Keysight) and fitted curves in two frequency ranges (pink dashed line: 1 kHz–100 kHz; blue solid line: 100 kHz–1 MHz). (b) Measured laser relative intensity noise. Blue line: measured noise with the laser frequency locked to the atomic resonance line, which is the sum of the AM–AM noise and the FM–AM noise. Red line: measured noise when the laser frequency is detuned away from the atomic resonance line, which is mainly AM–AM noise. Black line: measurement floor of the PD and the fast Fourier transform analyzer (SRS785, SRS) with no incident light.

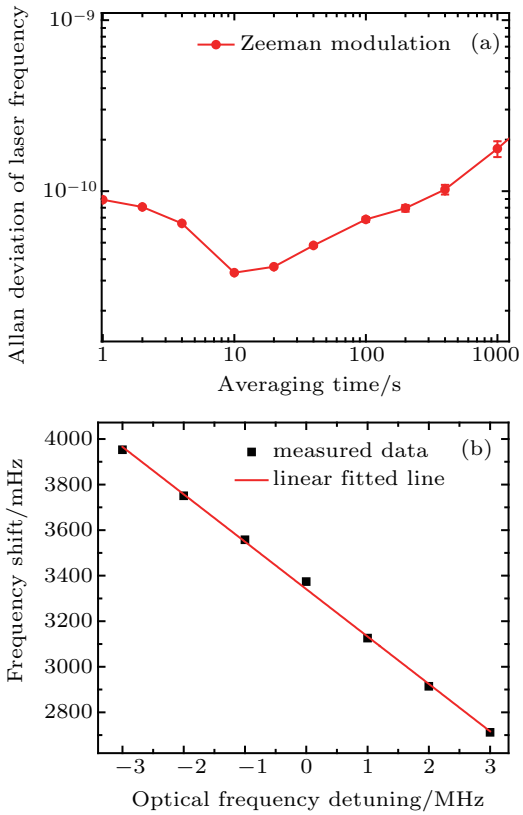


Fig. 11. (a) Measured laser frequency stability locked to the reference cell using Zeeman modulation. (b) Measured laser frequency-induced clock frequency shift (black squares) and corresponding linear fitted line (red line), which is mainly due to the AC Stark effect. The slope is measured to be −201 mHz/MHz.

The measured laser power stability is shown in Fig. 12(a). When the laser power stabilization loop is active, the in-loop stability reaches 5×10^{-6} at 1 s and stays below 8×10^{-6} up to 1000 s. However, the out-loop stability reaches 6.6×10^{-6} at 1 s and deteriorates to 1.0×10^{-5} at 100 s. If the laser stabilization loop turns off, the in-loop and out-loop laser power stabilities show the same Allan deviation results, which deteriorate from 1.8×10^{-4} on a slope of approximately $\sqrt{\tau}$. With the help of the laser power stabilization procedure, the laser intensity noise is reduced by a factor of 25. Note however that the power stability of the pulsed laser beam when interacting with the atoms is slightly worse than the measured result because of the process of switching on and off performed by AOM3. The slope of the laser intensity-induced clock frequency shift is measured to be −1.27 Hz/mW at 37.5 °C, as shown in Fig. 12(b). The derived frequency stability limitation of the laser intensity instability is 2.2×10^{-15} at 1 s and is 3.3×10^{-15} at 100 s.

To reduce the number of wall collisions and the Doppler broadening, the vapor cell is filled with buffer gases. However, the clock frequency is then shifted by the collisions between the buffer gases and the Cs atoms. In a sealed vapor cell, the collision intensity is mainly dependent on the cell temperature. Therefore, the cell temperature fluctuations perturb the clock transition stability. Fortunately, the collision-related shift can be minimized by filling the cell with two types of buffer gas, as mentioned in Section 2.2. As shown in Fig. 13(a), the cell temperature stability is measured to be 2.21×10^{-5} at 1 s and 1.07×10^{-5} at 100 s. The slope of the clock frequency shift versus temperature characteristic is measured to be −3.6 Hz/K, as shown in Fig. 13(b). Therefore, the frequency stability limitation due to the collision frequency shift is determined to be 8.7×10^{-15} at 1 s and 4.2×10^{-15} at 100 s.

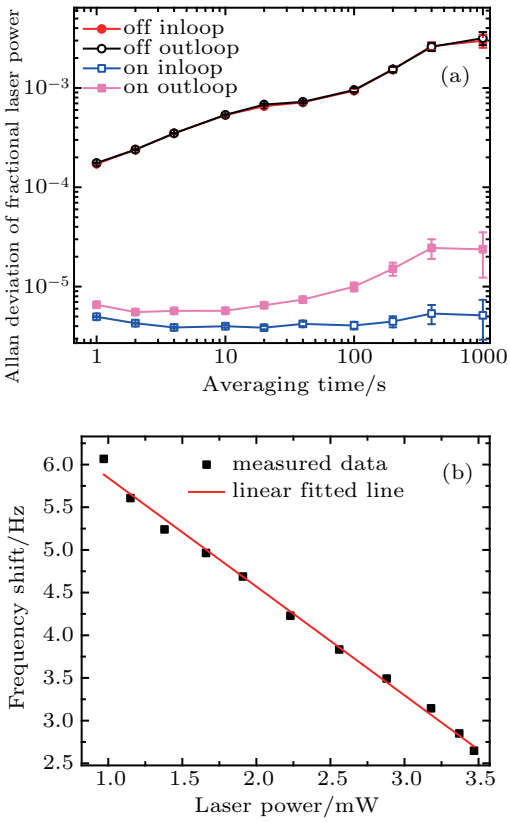


Fig. 12. (a) Measured laser power stability of the in-loop and the out-loop. (b) Measured laser power-induced clock frequency shift (black squares) and corresponding linear fitted line (red line); this shift is mainly due to the AC Stark effect. The slope is measured to be −1.27 Hz/mW.

The magnetic field (B) applied to the Cs atoms is expected to induce a shift via the Zeeman effect, which is expressed in terms of second-order sensitivity as follows:

$$\delta\nu_B = \alpha_B B \delta B, \tag{9}$$

where $\alpha_B = 42.7$ mHz/μT^2, δB represents the fluctuations of the magnetic field B, and B is optimized to have a value of 10 μT. As noted in Section 2.2, the residual magnetic field in the shield and the heating-current-induced magnetic field are both significantly smaller than the C-field. The stability of the C-field is determined by measuring the solenoid-driven current. As shown in Fig. 14(a), the results at 1 s and 100 s are 1.19×10^{-4} μT and 1.12×10^{-5} μT in terms of the Allan

deviation, respectively. We have also measured the value of α_B experimentally to be 48.0 mHz/μT^2, which is close to the theoretically calculated value of 42.7 mHz/μT^2. As a result, the frequency stability limitation due to the quadratic Zeeman shift induced in the clock is 1.3×10^{-14} at 1 s and 1.1×10^{-15} at 100 s.

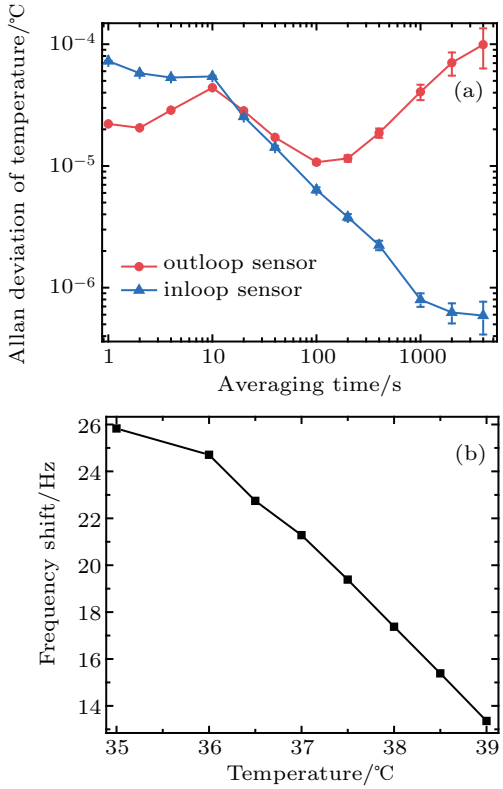


Fig. 13. (a) Measured cell temperature stability. The out-loop sensor is an extra negative temperature coefficient resistor (NTC) placed near the cell, and the stability is better than 0.1 mK up to 4000 s. (b) Measured temperature-induced frequency shift, which has a slope of approximately −3.6 Hz/°C.

The results of the above analyses are listed in Table 2. The largest noise source is the laser frequency noise and fluctuations. The laser frequency affects the 1 s stability through the FM–AM conversion, while it affects the 100 s stability through the light shift. The laser power noise and cell temperature-induced frequency stability limitations at 100 s are of secondary significance, while the magnetic noise is small enough to be neglected at that point. The total contributions of 1.6×10^{-12} at 1 s and 3.52×10^{-13} at 100 s are very close to the measured results of 1.3×10^{-12} at 1 s and 3.3×10^{-13} at 100 s, respectively. The laser frequency noise is mainly caused by the high sensitivity of the DBR laser to the injected current (1.14 GHz/mA) and the current noise of the current source (LDC205, SRS). Additionally, the poor medium-term laser frequency stability performance is attributed to the Zeeman modulation locking method, in which the saturation absorption spectrum is polarization-sensitive and varies with the room temperature. When the laser frequency stability is improved by one order of magnitude, the clock stability due to the laser frequency can be reduced to $5\times10^{-13}/\sqrt{\tau}$.

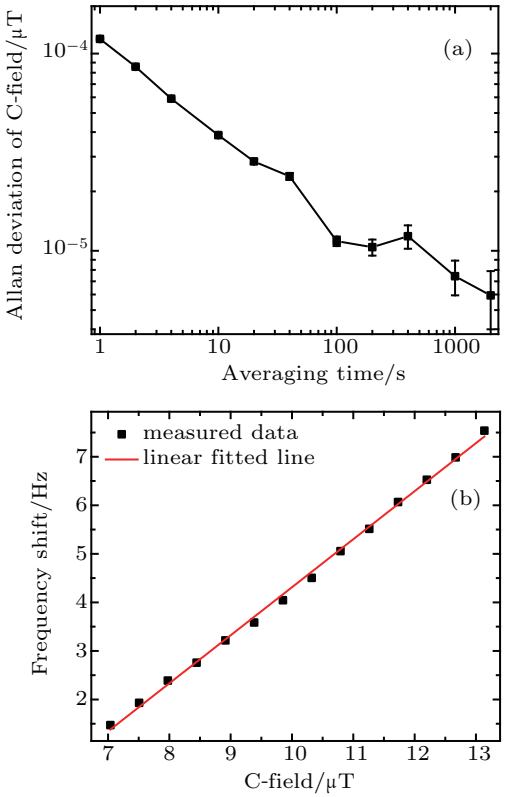


Fig. 14. (a) Stability of the magnetic C-field. The C-field value is calculated by measuring the drive current of the solenoid, which generates 2.346 μT/mA. (b) Measured magnetically-induced clock frequency shift due to the second-order Zeeman shifts of the related energy levels. The measured data (black squares) are fitted approximately linearly (red line) in a small interval around 10 μT, and the coefficient of the Zeeman shift is then calculated to be 48.0 mHz/μT^2, which is close to the theoretical value of 42.7 mHz/μT^2.

Table 2. Noise sources and their contributions to the Allan deviation.

Noise source-physical effect	σ_y (1 s)	σ_y (100 s)
Shot noise	4.3×10^{-14}	4.3×10^{-15}
Dick effect	5.1×10^{-13}	5.1×10^{-14}
FM–AM and AM–AM noises	1.5×10^{-12}	1.5×10^{-13}
Laser frequency noise-(light shift)	4.5×10^{-13}	3.5×10^{-13}
Laser power noise-(light shift)	2.2×10^{-15}	3.3×10^{-15}
Cell temperature noise-(collision shift)	8.7×10^{-15}	4.2×10^{-15}
Magnetic noise-(2nd order Zeeman shift)	1.3×10^{-14}	1.1×10^{-15}
Total $\sqrt{\sum_i \sigma_{y_i}^2(\tau)}$	1.6×10^{-12}	3.8×10^{-13}
Measured $\sigma_y(\tau)$	1.3×10^{-12}	3.3×10^{-13}

4. Conclusions

We demonstrate a Cs Ramsey-CPT atomic clock based on the lin||lin scheme with a dispersion detection technique. We have thoroughly optimized the related parameters, including the laser power, the angle of the two Glan–Taylor polarizers, the cell temperature, the quantizing magnetic field, the RF power, and the timing sequences. To date, the clock frequency stability has been measured to be $1.6\times10^{-12}/\sqrt{\tau}$ up to 20 s, and reaches 3.1×10^{-13} at 200 s. From investigations of the frequency limitations at 1 s and 100 s, the laser

frequency noise is found to be the most significant issue that limits the frequency stability via FM–AM conversion and light shifting effects. The results of these analyses indicate a way to improve the laser frequency stabilization setup, from which a promising stability performance of $5 \times 10^{-13}/\sqrt{\tau}$ is expected.

References

[1] Mallette L A, Rochat P and White J 2006 *Proceedings of the 38th Annual Precise Time and Time Interval (PTTI) Meeting*, December 7–9, 2006 Reston, USA, pp. 69–80

[2] Vanier J 2005 *Appl. Phys. B* **81** 421

[3] Alzetta G, Gozzini A, Moi L and Orriols G 1976 *Il Nuovo Cimento B (1971–1996)* **36** 5

[4] Yun P, Tricot F, Calosso C E, Micalizio S, François B, Boudot R, Guérandel S and de Clercq E 2017 *Phys. Rev. Applied* **7**

[5] Zanon T, Guérandel S, de Clercq E, Holleville D, Dimarcq N and Clairon A 2005 *Phys. Rev. Lett.* **94** 193002

[6] Taichenachev A V, Yudin V I, Velichansky V L and Zibrov S A 2005 *J. Exp. Theor. Phys. Lett.* **82** 398

[7] Jau Y Y, Miron E, Post A B, Kuzma N N and Happer W 2004 *Phys. Rev. Lett.* **93** 160802

[8] Zibrov S A, Novikova I, Phillips D F, Walsworth R L, Zibrov A S, Velichansky V L, Taichenachev A V and Yudin V I 2010 *Phys. Rev. A* **81**

[9] Warren Z, Shahriar M S, Tripathi R and Pati G S 2017 *Metrologia* **54** 418

[10] Sanner C, Huntemann N, Lange R, Tamm C and Peik E 2018 *Phys. Rev. Lett.* **120** 053602

[11] Liu X, Merolla J M, Guérandel S, de Clercq E and Boudot R 2013 *Opt. Express* **21** 12451

[12] Hafiz M A, Coget G, Petersen M, Rocher C, Guérandel S, Zanon-Willette T, de Clercq E and Boudot R 2018 *Phys. Rev. Applied* **9** 064002

[13] Yano Y and Goka S 2014 *IEEE Trans. Ultrason. Ferroelectr. Freq. Control* **61** 1953

[14] Sun X L, Zhang J W, Cheng P F, Xu C, Zhao L and Wang L J 2016 *Opt. Express* **24** 4532

[15] Tan B, Tian Y, Lin H, Chen J and Gu S 2015 *Opt. Lett.* **40** 3703

[16] Cheng P F, Sun X L, Xu C, Gao C, Zhao L, Zhang J W and Wang L J 2016 *Proceedings of the IEEE International Frequency Control Symposium (IFCS)*, May 9–12, 2016 New Orleans, USA, p. 1

[17] Danet J M, Kozlova O, Yun P, Guérande S and de Clercq E 2014 *Proceedings of the EPJ Web of Conferences* **77** 00017

[18] Kozlova O, Danet J M, Guérandel S and de Clercq E 2014 *IEEE Trans. Instrum. Meas.* **63** 1863

[19] Tricot F, Phung D H, Lours M, Guérandel S and de Clercq E 2018 *Rev. Sci. Instrum.* **89** 113112

[20] Ramsey N F 1949 *Phys. Rev.* **76** 996

[21] Kozlova O, Guérandel S and de Clercq E 2011 *Phys. Rev. A* **83** 062714

[22] Santarelli G, Audoin C, Makdissi A, Laurent P, Dick G J and Clairon A 1998 *IEEE Trans. Ultrason. Ferroelectr. Freq. Control* **45** 887

[23] Micalizio S, Calosso C E, Godone A and Levi F 2012 *Metrologia* **49** 425

[24] Cheng P F, Sun X L, Liu F W, Zhang D, Zhang J W and Wang L J 2017 *Proceedings of the IEEE International Frequency Control Symposium (IFCS)*, July 9–13, 2017 Besancon, France, pp. 616–617

[25] Camparo J C 1998 *J. Opt. Soc. Am. B* **15** 1177

[26] Camparo J C and Coffer J G 1999 *Phys. Rev. A* **59** 728